06

Determination of the Band Structure and Conductivity of the Si@O@Al Nanocomposite

© A.S. Rudy, A.B. Churilov, S.V. Kurbatov, A.A. Mironrenko, V.V. Naumov, E.A. Kozlov

Demidov State University,
150003 Yaroslavl, Russia
e-mail: rudy@uniyar.ac.ru, abchurilov@mail.ru, kurbatov-93@bk.ru

Received April 16, 2023
Revised July 27, 2023
Accepted July 31, 2023

The purpose of this work is to study the characteristics of the junction between the titanium down conductor of a thin-film solid-state lithium-ion battery (a-Si) and a negative Si@O@Al nanocomposite electrode. The results of measuring the band gap of the Si@O@Al nanocomposite and the height of the Schottky barrier of the Ti-Si@O@Al junction are presented. The transmission and reflection spectra of Si@O@Al films and its main phases a-Si, a-SiO_x and a-$Si(Al_x)$ are studied. The band gap of Si@O@Al was determined by the Tauc method, which is 1.52 eV for a-Si and 1.15 eV for nc-Si. The IV characteristics of Ti—Si@O@Al, Ti—a-Si, Ti—a-SiO0.8, and Ti—a-Si0.9(Al0.1) structures have been studied and the height of the Schottky barrier has been determined. The results obtained make it possible to estimate the Fermi energy of the nanocomposite and to interpret the hike in the SSLIB charging voltage as a result of the Al acceptor impurity compensation during lithiation. A change in the majority charge carriers in Si@O@Al leads to a decrease in the hole current and an increase in the density of the over-barrier electron current, as a result of which a step with a height of 1.5 V is formed on the charging curve.

Keywords: nanocomposite, amorphous silicon, solid solution, optical band gap, Tauc plot, current-voltage characteristic, Schottky barrier, electron affinity, varistor effect.

DOI: 10.61011/TP.2023.10.57451.93-23

Introduction

One of the most promising materials for the negative electrode of solid-state thin-film lithium-ion batteries (STLIB) is the Si@O@Al nanocomposite. In the structure of STLIB, the functional layers Si@O@Al and Ti (current collector) form the transition metal−semiconductor. The charge-discharge curves of such STLIB and current-voltage curve of the Ti−Si@O@Al transition have a number of features, the interpretation of which is impossible without involving the Si@O@Al band structure. The purpose of this work is to determine the parameters of the band structure and the main mechanisms of charge transfer of the Si@O@Al nanocomposite and its forming phases in the volume and in the area of contact with the titanium current collector.

The history of modern STLIB dates back to the mid-90s, when the solid electrolyte — lithium phosphorus-oxynitride or LiPON [1] was developed. The first STLIB had almost the same electrochemical system as modern batteries. Along with LiPON, lithium cobaltite $LiCoO_2$ was used as a positive electrode, and in as a negative — lithium metal or graphite. These materials have a number of disadvantages, for example, the theoretical specific capacity of graphite is relatively small and is only 372 mA · h. As for lithium, with a large theoretical capacity of 3828 mA · h/g, its practical capacity is only 380−800 mA · h/g. The reason lies in the encapsulation of lithium, i.e. the formation of a passivating film around lithium crystallites when charged. In addition, batteries with metallic lithium are not safe to use.

Therefore, the search for alternatives to graphite and lithium continues today and, most likely, silicon will replace them over time. This material with the least densely packed crystal lattice (packing coefficient $P = (\sqrt{3}\pi/16) \cdot 100\% = 34\%$), has a record theoretical capacity relative to the reversible introduction of lithium 4200 mA · h/g. Theoretically, a silicon atom can attach up to four lithium atoms to form an intermetallic compound $Li_{22}Si_5$. This does not happen in practice, because crystalline silicon is destroyed by internal stresses despite the low packing density long before the appropriate stoichiometry is achieved.

A nanocomposite material was developed to increase the stability of the silicon-based electrode Si@O@Al [2,3]. Here, in accordance with established practice, the sign *at sign* or @ is used to denote a composite material. With magnetron deposition, the capacity of Si@O@Al can be adjusted from 1000 to 3000 mA · h/cm^2, it withstands more than 1000 charge−discharge cycles and can be stored in air for several years. However, with all the advantages of Si@O@Al, there is a step on the plateau of the STLIB charging curve (Fig. 1), called a„hike“ in English literature. Such a charging curve is quite common in batteries with liquid electrolyte. For solid-state thin-film lithium-ion batteries (LIB), the curve with „haikom“ is always an undesirable phenomenon, indicating the appearance of additional internal resistance. It is characteristic that the step is fully manifested only in cells with a high-capacity cathode (for example, with higher vanadium oxides). On the charging curve of a cell with lithium cobalt, only the

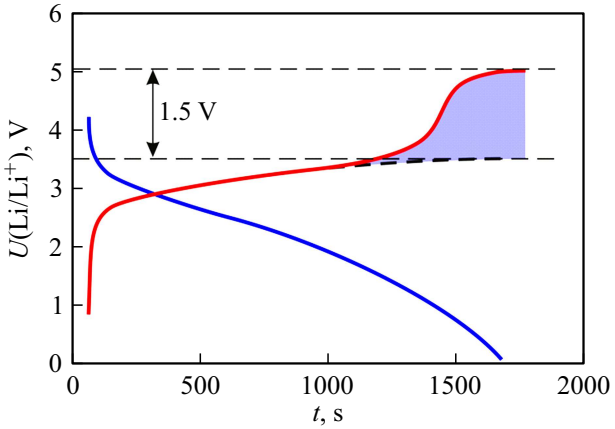

Figure 1. The charge-discharge curve of a battery cell with the structure Ti—Si@O@Al—LiPON—$Li_xV_2O_5$—Ti.

initial section of the step is present, since it is not possible to achieve a high level of anode lithium due to the small capacity of the cathode.

Paper [4] showed that a step on the charging curve appears as a result of a change in the type of conductivity Si@O@Al, which is a p-type semiconductor before lithiation, and as a result of compensation of the acceptor impurity Al with lithium becomes an n-type semiconductor. At the beginning of charging (anode lithiation), when Si@O@Al is a hole semiconductor, the charge is transferred by holes, and the current through the Ti—Si@O@Al contact has a recombination character. After changing the type of conductivity to electronic, the charge is transferred by electrons overcoming the Schottky barrier. As a result, the transition resistance increases, and a step appears on the charging curve in the galvanostatic charge mode (Fig. 1).

The paper [5] that studied current-voltage curve of the Ti—Si@O@Al—Ti test structure experimentally confirmed that the solid solution a-Si(Al), which forms the basis of the nanocomposite, is a hole semiconductor. At the same time, all estimates made in [4,5] were based on the assumption that the band structure of a-Si(Al) differs little from the band structure of a-Si. When estimating the height of the Schottky barrier, the following parameters were used: the width of the band $E_g = 1.18$ eV gap and electronic affinity $\chi = 2.38$ eV [6,7]. These data were obtained by calculation for the cluster a-Si (4096 atoms in [6] and 16 atoms in [7]). According to these data and taking into account the fact that the Fermi level of silicon E_{FS} is almost at the level of E_{VS} — the lower mobility threshold $E_{FS} \simeq E_{VS}$, the Fermi level a is Si(Al) at above the Fermi level Ti. In this case, there is a Schottky barrier with a height of $q\varphi_B = E_{FM} - \chi = 1.92$ eV in the contact area Ti—a-S(Al) on the metal side, and the model proposed in [4] is correct. However, E_g and χ of the Si@O@Al nanocomposite may differ significantly from the model parameters of a-Si. Therefore, the final conclusion about the mechanism of step formation on the charging curve (Fig. 1) can be made only on the basis of experimental values of the band gap width and the electron affinity of Si@O@Al and its main phases.

Below is a description of the manufacture of test structures from Si@O@Al nanocomposite and its main phases a-Si, a-$Si_{0.9}(Al_{0.1})$ and $SiO_{0.8}$, and also methods and results of determining the width of the forbidden zone by the Tauc method (Jan Tauc) [8]. The following are the current-voltage curves, according to which the height of the Schottky barrier of silicon-containing phases and their electronic affinity are calculated. These results confirm the mechanism and clarify the parameters of the dependence of the Si@O@Al resistance on the state of charge of the battery and can be used in the design of STLIB and the development of an algorithm for controlling the charge–discharge process.

1. Production of experimental samples

Experimental samples were made in the form of Si@O@Al films with a thickness of ~ 100 and ~ 200 nm (samples SiOAl-100 and SiOAl-200, respectively) deposited on substrates of fused quartz of the CU1 brand with a diameter of 40 mm and 1.1 mm thick (Fig. 2) for measuring the width of the band gap.

The films were applied by RF magnetron sputtering of a target of the composition $Si_{0.9}Al_{0.1}$ in the unit SCR-651 „Tetra“. Samples of films of the composition$a$-Si, a-$Si_{0.9}(Al_{0.1})$ and a-$SiO_{0.8}$ were made at the unit. All samples were made without heating the substrate during application, without displacement on the substrate and under pressure 1.75 Pa. When applying a-Si films, pure silicon was used as a target. The film a-$Si_{0.9}(Al_{0.1})$ was applied by spraying a mosaic target $Si_{0.9}Al_{0.1}$ without oxygen supply. The technological parameters of the film application are given in Table 1.

Witness–samples were made simultaneously with them to determine the elemental composition of the films. Their elemental composition was controlled by energy dispersive microanalysis on an EDAX attachment to a Quanta 3D200i microscope. In order to minimize the signal from the substrate, the analysis was carried out at a low electron beam energy of 4 kV. Atomic ratios of elements normalized by 100% are presented in Table. 2. The thickness of the film on all samples was determined by the thickness of the film on the chip of the corresponding sample– of the witness using a scanning electron microscope Supra 40 (Carl Zeiss).

Ti—Si@O@Al—Ti, Ti—Ti test structures were made to study the current-voltage curve of nanocomposite Si@O@Al, amorphous silicon, solid solution a-$Si_{0.9}(Al_{0.1})$ and silicon oxide$a$-Si—Ti, Ti—a-$Si_{0.9}(Al_{0.1})$—Ti and Ti—$SiO_{0.8}$—Ti. The technology of their manufacture differed from the one described above only in that the manufacturing process began and ended with the operation of applying titanium layers. The cleavage of the Ti—Si@O@Al—Ti test structure and layer thicknesses are shown in Fig. 2.

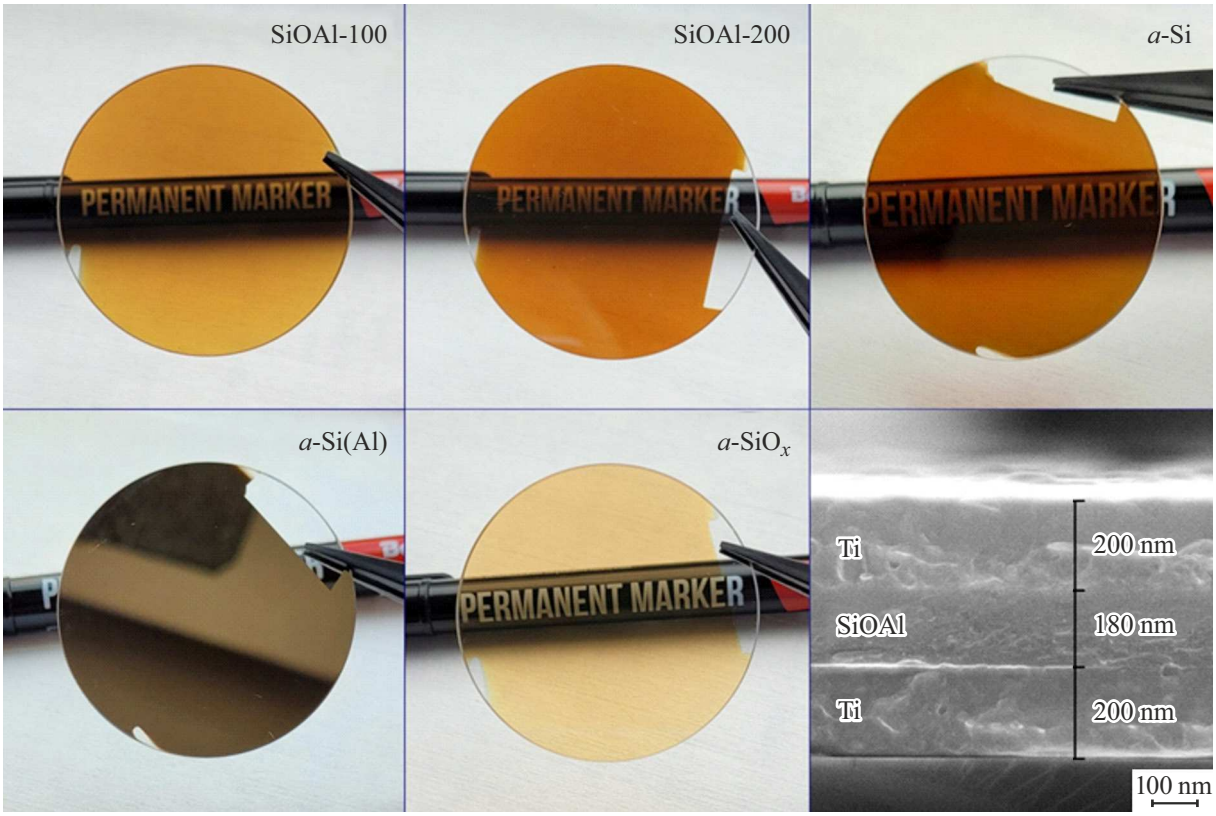

Figure 2. Films Si@O@Al, a-Si, a-$Si_{0.9}(Al_{0.1})$ and a-$SiO_{0.8}$ on a substrate of fused quartz and SEM, an image of a chip of the Ti—Si@O@Al—Ti structure on a silicon substrate. The elemental composition of the films is shown in Figure and in Table. 2.

Table 1. Main parameters of magnetron film deposition

Specimen	SiOAl-100	SiOAl-200	a-Si	a-$Si_{0.9}(Al_{0.1})$	a-$SiO_{0.8}$
Gas consumption, sccm*	Ar, 200 O_2, 0.6	Ar, 200 O_2, 0.6	Ar, 200	Ar, 200	Ar, 200 O_2, 0.6
Application time , min	2	4	4	4	4
Thickness	100 nm	200 nm	200 nm	200 nm	200 nm

Note. *sccm — ml/min at 0°C, 101.3 kPa.

Table 2. Elemental analysis of the film Si@O@Al

Element	at.%	Δ at.%
O, K_α	24.3	0.3
Al, K_α	16.8	0.2
Si, K_α	58.9	0.5

2. Measurement of transmittance and reflectance spectra

A single-channel spectrophotometer SF-56 (LOMO) with a range of 200−1100 nm was used to measure the transmittance of all films. The reflection coefficient at normal light incidence was measured using an optical microscope Leitz MPV-SP with a built-in monochromator in the spectral range 400−800 nm with a resolution of 1 nm. The transmittance spectrum $T(\lambda)$ was measured in the range of 200−1100 nm. The spectra of a quartz substrate were recorded to control the calibration during the measurement of the characteristics of the SiOAl-100 and SiOAl-200 samples. The results obtained are shown in Fig. 3, *a*.

The reflection spectra of the samples were studied in the range from 400 to 800 nm with 1 nm increments. The microscope was calibrated using a polished silicon wafer as a reference with a known dependence of the reflection coefficient $R_{Si}(\lambda)$ [9]. The absolute values of the reflectance $R_x(\lambda)$ were calculated using the measurement results in relative units R_x/R_{Si} taking into account the calibration results as the product of (R_x/R_{Si}) and $R_{Si}(\lambda)$

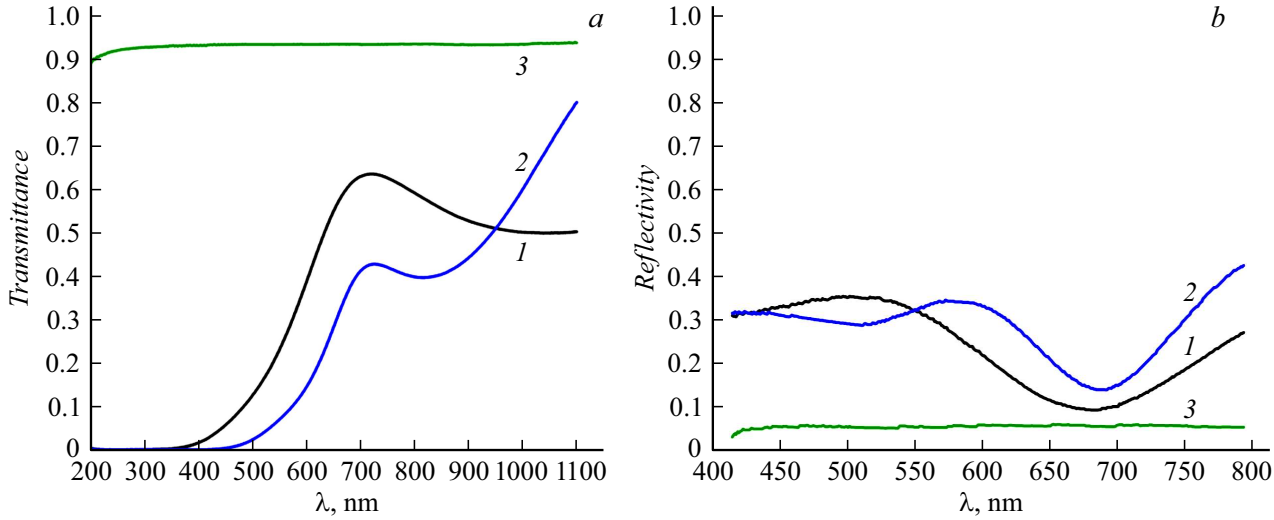

Figure 3. Transmittance spectra (a) and reflection (b) of films and quartz substrates: *1* — SiOAl-100, *2* — SiOAl-200, *3* — quartz.

for each wavelength. The dependencies $R_x(\lambda)$ in the range from 400–800 nm are shown in Fig. 3, *b*. The transmittance of quartz grade KU1 lies within $T = 0.93–0.99$ for the spectral range 210–1000 nm [10].

The transmittance coefficients (curve *3* in Fig. 3, *a*) and reflection (curve *3* in Fig. 3, *b*) of quartz plates were measured to verify the reliability of the results. The resulting values $T \approx 0.93$ and $R \approx 0.06$ add up to $T + R \approx 0.99$ — a value close to unity. Thus, measurements on each of the devices give reliable absolute values of transmittance and reflection coefficients. These results allow calculating the absorption coefficient of films and determine the band gap width by the method described below.

3. Determining the width of the band gap

The film-substrate structure has three boundaries: air–film, film–substrate and substrate–air with its own reflection coefficients. Due to multiple reflections from the boundaries and interference, the calculation of the optical constants of a thin film becomes more complicated. A strict derivation of formulas for calculating the absorption coefficient can be found in the literature [11,12]. Under the condition of strong absorption in the film and negligible absorption in the substrate, which is most often realized in practice, the absorption coefficient of the film α_{film} can be calculated using the simplified formula [13]:

$$\alpha_{\text{film}} = \frac{1}{d_{\text{film}}} \ln \frac{(1-R_1)(1-R_2)(1-R_3)}{T_{\text{tot}}}, \qquad (1)$$

where d_{film} — film thickness, R_1, R_2 and R_3 — reflection coefficients at the boundary air–film, film–substrate and substrate–air respectively and T_{tot} — transmittance coefficient through the film–substrate structure. However, the reflection at the boundary of the film–substrate R_2 in the formula (1) most often it is not known before the experiment. The ratios obtained for a free film (without substrate) [14,15] are used to calculate the absorption coefficient in this case. Under the condition of $T_{\text{tot}} > 10\%$, the absorption index can be represented as

$$\alpha_{\text{film}} = \frac{1}{d_{\text{film}}} \ln\left(\frac{(1-R_{\text{tot}})^2}{2T_{\text{tot}}} + \sqrt{\frac{(1-R_{\text{tot}})^4}{4T_{\text{tot}}^2} + R_{\text{tot}}^2}\right), \qquad (2)$$

and under the condition of strong absorption, when $T_{\text{tot}} < 10\%$, the last term can be neglected:

$$\alpha_{\text{film}} = \frac{1}{d_{\text{film}}} \ln \frac{(1-R_{\text{tot}})^2}{2T_{\text{tot}}}. \qquad (3)$$

Here R_{tot} and T_{tot} — experimental values of reflectance and transmittance of the film structure–substrate. Examples of using the formula (2) to calculate the absorption index of TiN, CdTe, ZnSe films of various thicknesses ($\sim$ 100–600 nm) can be found in [16,17].

Another approach was proposed by the authors of [18], where the absorption index of the film is calculated by formula

$$\alpha_{\text{film}} = \frac{d_{\text{sub}}}{d_{\text{film}}} \ln(\alpha_{\text{tot}} - \alpha_{\text{sub}}), \qquad (4)$$

and the absorption indices of the substrate α_{sub} and the structure of the film–substrate α_{tot} are calculated as

$$\alpha_{\text{sub}} \approx \frac{1}{d_{\text{sub}}} \ln\left(\frac{1-R_{\text{sub}}}{T_{\text{sub}}}\right), \qquad (5)$$

$$\alpha_{\text{tot}} \approx \frac{1}{d_{\text{film}} + d_{\text{sub}}} \ln\left(\frac{1-R_{\text{tot}}}{T_{\text{tot}}}\right), \qquad (6)$$

where R_{tot} and T_{tot} — the reflectance and transmittance coefficients of the film system–substrate, T_{sub} — transmittance coefficient of the substrate and R_{sub} — coefficient of reflectance from the substrate. Formulas (4)–(6) directly

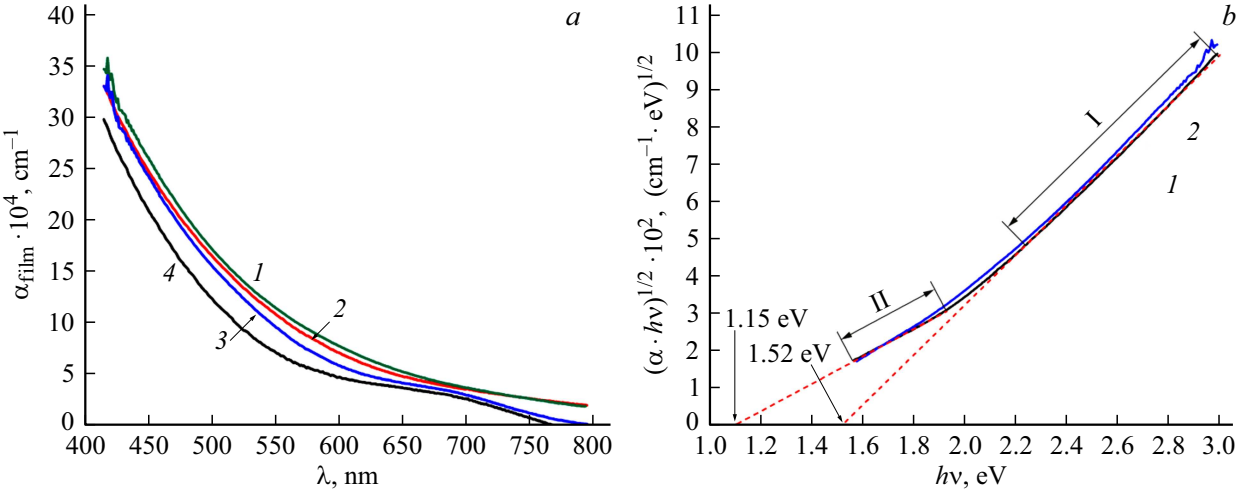

Figure 4. *a* — absorption coefficients of Si@O@Al films calculated using formulas (4)–(6): *1* — SiOAl-200, *2* — SiOAl-100 and by formulas (2), (3): *3* — SiOAl-200, *4* — SiOAl-100; *b* — Tautz's plots for samples SiOAl-200 (curve *1*) and SiOAl-100 (curve *2*) with extrapolation of linear sections.

follow from Booger–Lambert laws without taking into account secondary reflections and are valid only for a single-pass scheme. At the same time, a single-pass scheme can introduce a significant error in the calculation of the absorption index and, as a consequence, in the optical band gap, especially for films thinner than 100 nm [17].

Fig. 4, *a* shows the spectral dependences of the absorption coefficients of films calculated by formulas (2), (3) and (4)–(6). The calculation in the first way gives smaller values of the absorption coefficient (curves *3, 4* compared to the dependencies *1, 2*). Next, the second method (of the formula (4)–(6)) was used to calculate the optical band gap.

The dependence proposed by Tautz [8,19] is used for the experimental determination of E_g in amorphous semiconductors in the case of indirect allowed transitions:

$$(\alpha_{film} \cdot h\nu)^{1/2} = B(h\nu - E_g), \qquad (7)$$

where $h\nu$ — photon energy corresponding to the wavelength of incident radiation, B — Tautz's parameter. Sometimes the parameter B is associated with the degree of ordering in amorphous and polycrystalline materials [20]. The linear section on the dependence of $(\alpha_{film} \cdot h\nu)^{1/2}$ on $h\nu$ is extrapolated to the intersection with the energy axis to determine E_g. The intersection point gives the desired value E_g, since at $\alpha = 0$ the equality $h\nu = E_g$ takes place. In turn, the tangent of the angle of inclination of the straight line is equal to the Tautz's parameter B.

Fig. 4, *b* presents experimental dependencies $f(h\nu) = (\alpha_{film} \cdot h\nu)^{1/2}$ calculated by formula (4). Two areas designated as I and II are clearly distinguishable on dependencies. Area I — extended almost linear section belonging to the segment $h\nu > 2.2$ eV, area II — short linear section $h\nu < 2.0$ eV. These plots were approximated by a linear dependence $f(h\nu) = a(h\nu) + b$, the parameters of which were selected by the least squares method. Extrapolation of linear sections I gives the following values:

$$\text{for sample SiOAl} - 100: \; E_{g1} = 1.52 \pm 0.01 \text{ eV}$$

$$\text{and } B_1 = 667.7 \text{ cm}^{-1/2} \cdot \text{eV}^{-1/2};$$

$$\text{for sample SiOAl} - 200: \; E_{g1} = 1.52 \pm 0.01 \text{ eV}$$

$$\text{and } B_2 = 679.6 \text{ cm}^{-1/2} \cdot \text{eV}^{-1/2};$$

which is very close to the literature data. For example, for *a*-Si $E_g = 1.55$ eV [21]. Extrapolation of linear section II gives the value $E_{g2} = 1.15 \pm 0.01$ eV, on the basis of which section II can be attributed to the contribution to absorption due to nanocrystalline silicon. The presence of a small fraction of silicon nanocrystallites in the Si@O@Al nanocomposite is confirmed by the data of X-ray phase analysis of [22] and the results of this study. There should be a section of the spectrum in area $h\nu < E_{g2}$, according to [23] caused by structural defects belonging to the grain boundary. However, judging by the results obtained, this area is significantly below the value of E_{g2} and does not fall within the measurement range.

For a confident interpretation of the Tautz's graphs for the Si@O@Al nanocomposite, it was necessary to compare them with the corresponding graphs for the compounds that make up the nanocomposite. Dependence plots $f(h\nu) = (\alpha_{film} \cdot h\nu)^{1/2}$ for films *a*-Si, *a*-$SiO_{0.8}$, *a*-$Si_{0.9}(Al_{0.1})$ are shown in Fig. 5. The Tautz's plot for *a*-$SiO_{0.8}$ is the same as the plot in Fig. 4, *b*, consists of two linear regions. The region with the maximum band gap $E_{g3} = 1.89 \pm 0.01$ eV, most likely corresponds to absorption in SiO_2, whereas the region with $E_{g2} = 1.15 \pm 0.04$ eV refers to *nc*-Si. This is indicated by the coincidence of the intersection points of the Tautz line plots for *a*-Si and *a*-$SiO_{0.8}$ with the abscissa axis (Fig. 5). This result is quite natural, since the deposition conditions of these films differ only in the oxygen

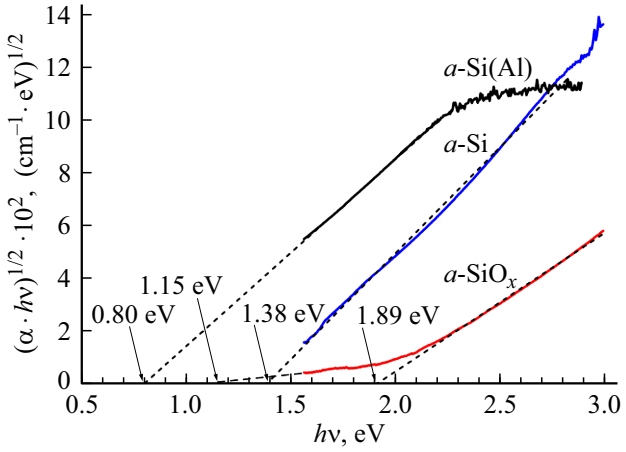

Figure 5. Tautz's graphs for films a-Si, a-$SiO_{0.8}$, a-$Si_{0.9}(Al_{0.1})$.

intake during magnetron deposition a-$SiO_{0.8}$ (Table 1). Amorphous silicon is formed a-$SiO_{0.8}$, consisting of a matrix a-Si with the nanoclusters SiO_2 and nc-Si included in it.

It was noted in [24] that the presence of silicon nanoclusters a-Si:H in films a-SiO_x:H should lead to an increase of the density of the allowed states above the ceiling of the valence band E_V, which for SiO_2 is ~ 6 eV. That is, an increase of the concentration of nanoclusters a-Si:H in the SiO matrix$_2$ should be accompanied by an increase of the ceiling of the valence band and a decrease of the band gap. The optical band gap in films a-SiO_x:H in work [24] is 3.2–3.3 eV at a fifty percent concentration of silicon nanoclusters. The opposite situation occurs in the subject case— the concentration of SiO_2 in a-Si is 10–15 mol.%, so the band gap a-$SiO_{0.8}$ is lower than the composite a-SiO_x:H and is 1.89 eV.

Extrapolation of the Tautz's plot for a-$Si_{0.9}(Al_{0.1})$ gives the value $E_{g3} = 0.8 \pm 0.003$ eV, which is less than the band gap of not only amorphous, but also crystalline silicon. One of the reasons for the narrowing of the band gap of the solid solution a-$Si_{0.9}(Al_{0.1})$ may be strong doping and even degeneration of the semiconductor. The obtained values of the band gap width allow constructing the band structure of Si@O@Al and the silicon-containing phases forming it, if the position of the upper boundary of the band or the electronic affinity is known. To determine the electronic affinity, the current-voltage curve test structures were used, the description and modeling of which is given in the next section.

4. Evaluation of the electronic affinity of films Si@O@Al, a-Si, $SiO_{0.8}$, a-$Si_{0.9}(Al_{0.1})$

Ti—Si@O@Al—Ti, Ti—a-$Si_{0.9}(Al_{0.1})$—Ti, Ti—a-Si—Ti and Ti—$SiO_{0.8}$—Ti tests structure were used to determine the electron affinity of Si@O@Al nanocomposite, solid solution a-$Si_{0.9}(Al_{0.1})$, amorphous silicon a-Si and silicon oxide a-$SiO_{0.8}$. Their current-voltage curves, obtained by cyclic voltammetry at a scanning speed of 5 mV/s, are shown in Fig. 6.

Due to the symmetry of the test structures, their current-voltage curve also have a symmetrical shape, although the resistances of metal–semiconductor and semiconductor–metal for the same polarity may differ greatly. If, according to [6,7], the work of the Fermi energy of titanium $E_{FM} = -4.3$ eV is modulo more than the Fermi energy of amorphous silicon E_{FS}, as shown in Fig. 7, a, then for hole silicon, the contact Ti—a-$Si_{0.9}(Al_{0.1})$ will be ohmic.

When offset in the forward direction (plus on the semiconductor), as shown in Fig. 7, c, the resistance of the Ti—Si@O@Al—Ti structure is determined only by the resistance of the nanocomposite volume, and current-voltage curve is linear. Thus, the current-voltage curve in Fig. 6 refers to a transition turned on in the reverse direction (plus on the metal), the current through which is created by non-primary charge carriers.

4.1. BAX Ti—Si@O@Al

The current-voltage curve Ti—Si@O@Al has the form of an exponent and, unlike the current-voltage curve of other test structures, does not contain a linear section. This means that the current through the inversely displaced junction has only one component — current through the Schottky barrier (SB). From this it follows that the density of localized states in Si@O@Al is very small, since otherwise there would be a linear tunneling current through traps (trap-assisted tunelling or TAT). This current is the main cause of leaks in the so-called MIM (Metal–Insulator–Metal) structures and gates of field-effect transistors. Band–to-band transitions are considered in a number of works devoted to TAT modeling, for example, in [25], where model current-voltage curves structures are given for AlGaN/GaN.

In the absence of TAT, the density of the total current through the transition metal–semiconductor can be represented in the form

$$I = I_S[\exp(q(U - U_V)/kT) - 1], \tag{8}$$

where $I_S = AT^2 \exp(-(q\varphi_B)/kT)$ — saturation current density, A — thermoelectric constant (Richardson constant), $q\varphi_B$ — height BS, U — offset voltage (Fig. 7, d), U_V — voltage drop on layer Si@O@Al [5]. Since the current-voltage curve in Fig. 6 has a nonlinear character, it is natural to assume that this is due to the nonlinearity of the resistance of the volume of the nanocomposite or the varistor effect. The nonlinear dependence of voltage on current can be described by the expression

$$U_V = R^* I^\alpha + R_0 I, \tag{9}$$

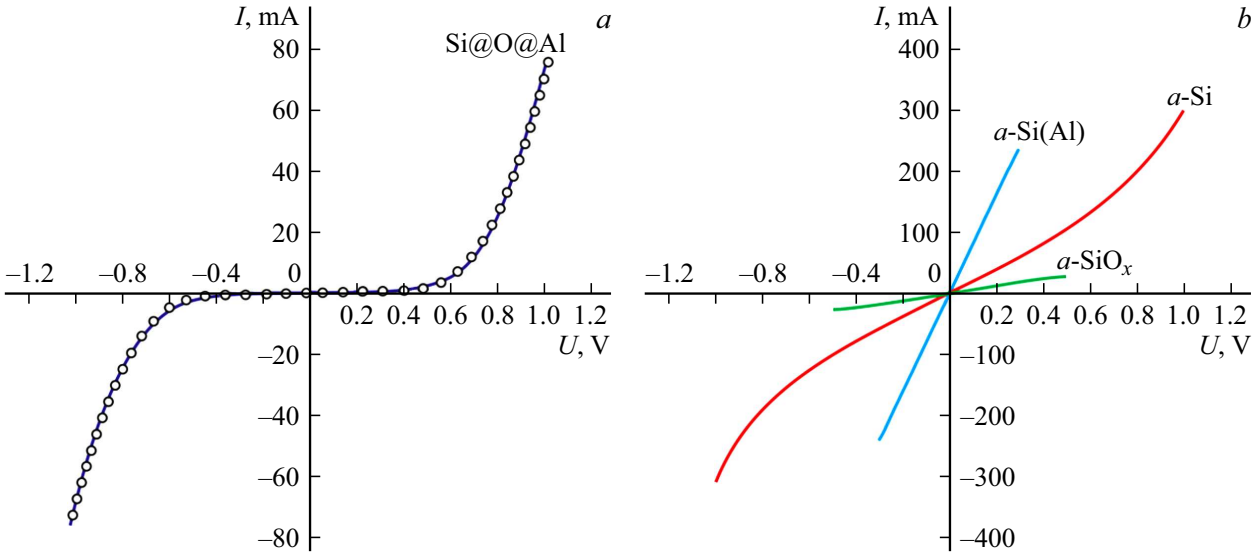

Figure 6. *a* — The current-voltage curve of the Ti—Si@O@Al—Ti test structure with an area of 1 cm^2 (solid curve) obtained at a scanning speed of 5 mV/s, and a dependence graph (*3*) (white circles) for the parameters $I_S = 10^{-10}\,\mathrm{A}\cdot\mathrm{cm}^{-2}$; $R^* = 1.56\,\Omega\cdot\mathrm{A}^{1-\alpha}$; $\alpha = 0.45$. *b* — Current-voltage curve of test structures *a*-Si (200 nm), *a*-$Si_{0.9}(Al_{0.1})$ (200 nm) and *a*-$SiO_{0.8}$ (200 nm).

where R^* — dimension coefficient $\Omega\cdot\mathrm{A}^{1-\alpha}$, R_0 — residual resistance, α — inverse value of the coefficient of nonlinearity of current-voltage curve

$$\beta = \frac{U}{I}\frac{dI}{dU}.$$

The residual resistance R_0 takes into account the obvious fact that at $\alpha < 1$ and $I \to \infty$ the resistance of the varistor is finite. The expression (7) will be as follows if the term $R_0 I$ is neglected due to its smallness

$$I = I_S[\exp\left(q(U - R^* I^\alpha)/kT\right) - 1]. \qquad (10)$$

The dependence (9) best approximates the experimental curve with the following parameters: $I_S = 10^{-10}\,\mathrm{A}\cdot\mathrm{cm}^{-2}$, $R^* = 1.56\,\Omega\cdot\mathrm{A}^{1-\alpha}$ and $\alpha = 0.45$.

The resistance of a material with a varistor effect depends on the current as $R = R^* I^{\alpha-1} + R_0$, which creates certain difficulties when compared with other materials. For certainty, it is possible to take the resistance value at a current of 1 A, then $R \approx R^* = 1.56\,\Omega$. This resistance corresponds to the conductivity $\sigma = 1.15\cdot 10^{-3}\,\mathrm{S}\cdot\mathrm{m}^{-1}$ and the parameter $\mu n = 7.2\cdot 10^{15}\,\mathrm{m}^{-1}\cdot\mathrm{V}^{-1}\cdot\mathrm{s}^{-1}$, where μ — mobility of holes, and n — their concentration. The value of the saturation current IS, allows calculating the height of the SB

$$\varphi_\mathrm{B} = \frac{kT}{q}\ln\left(\frac{\lambda_R A T^2}{I_S}\right) = 1.0\,\mathrm{eV}, \qquad (11)$$

where λ_R is a correction factor depending on the material, which usually has a magnitude of the order of 0.5. The corresponding value of the electron affinity can be found using the Schottky–Mott $\chi = A_M - q\varphi_\mathrm{B}$ rule, which in turn gives $\chi = 3.3$ eV. This result differs from these theoretical papers [6,7], where the value of the electron affinity of ~ 2.3 eV was obtained and which is closer to the generally accepted for *a*-Si:H value $\chi = 3.93$ [26].

It should be noted that due to a number of reasons (the strength of the electric image, the presence of surface states, etc.), the obtained value of the BS height may be underestimated, and the electronic affinity — overestimated. It should be also noted that in *a*-Si:H, the ceiling of the valence band is shifted down relative to *a*-Si due to the replacement of the Si–Si bond with a stronger Si–H bond. In solid solution *a*-$Si_{0.9}(Al_{0.1})$, this does not happen, so the increase of electron affinity relative to the model values of [6,7] should be attributed to a decrease of SB. Taking into account these observations, the obtained value of the electron affinity Si@O@Al should be considered as the upper limit, i.e. $\chi \le 3.3$ eV.

4.2. BAX Ti—*a*-Si

The current-voltage curve of the test structure Ti—*a*-Si—Ti in Fig. 6, *b* in contrast to the current-voltage curve in Fig. 6, *a* has a linear section in the range from −0.45 to +0.45 V. The presence of a linear section in the model under consideration is explained by the TAT effect, so further current-voltage curve on Fig. 6, *b* is considered as the sum of two currents $I = I_\mathrm{TAT} + I_\mathrm{ScB}$, where I_TAT — linear current through traps, and I_ScB — current through SB. The linear current is well approximated by the dependence $I_\mathrm{TAT} = CU + I_0$, where $C = 198.71\,\mathrm{mA}\cdot\mathrm{V}^{-1}$; $I_0 = 0.939$ mA. Subtraction of the linear dependence from the experimental $I(U)$ in Fig. 6, *b* gives a curve that has the form of an exponent. To approximate it, it is necessary

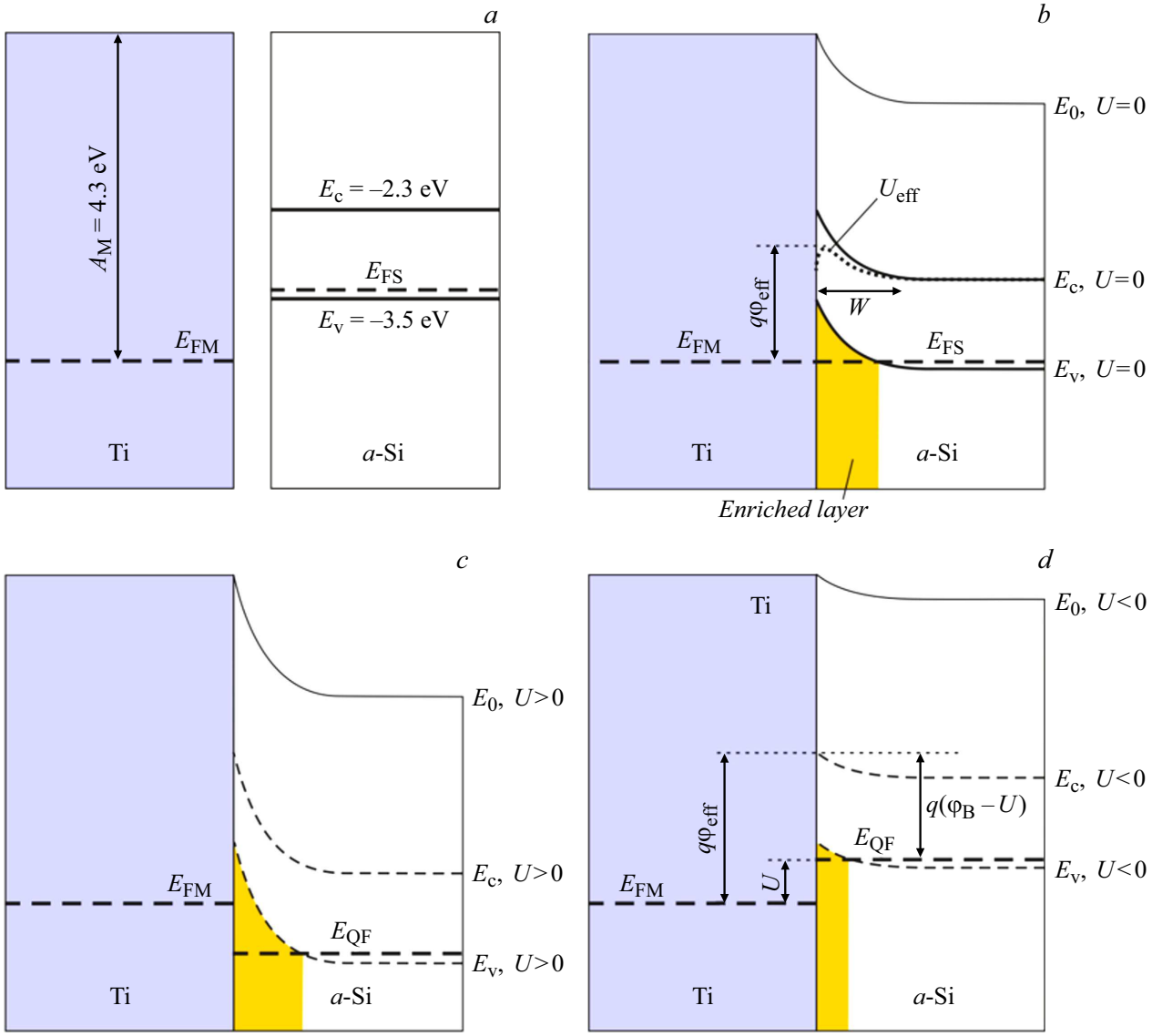

Figure 7. Band structure of the contact Ti—a-$Si_{0.9}(Al_{0.1})$: a — the band structure of Ti and a is $Si_{0.9}(Al_{0.1})$, where a-$Si_{0.9}(Al_{0.1})$ — solid substitution solution with low density of localized states; b — band structure of the contact Ti—a-$Si_{0.9}(Al_{0.1})$ without displacement; c — band structure Ti—a-$Si_{0.9}(Al_{0.1})$ with a forward displacement (plus by a-$Si_{0.9}(Al_{0.1})$); d — when the contact is reversed (minus by a-$Si_{0.9}(Al_{0.1})$); A_M — metal work function; E_{FM} — metal Fermi level, E_{FS} — semiconductor Fermi level; E_{QF} — quasi-level Fermi a-$Si_{0.9}(Al_{0.1})$; E_0 — vacuum level; E_c — bottom of conduction band; E_V — valence band ceiling; U — voltage displacement.

to find the dependence of the current through the SB on the voltage on the entire test structure $I_{ScB}(U)$. An equivalent scheme shown in Fig. 8, a was used to do this. According to the scheme, the resistance of the layer a-Si with a width of L consists of the resistance of the layer with a width of $L-W$ and the resistance of the space charge region (SCR) with a width of W and can be represented as $R_V = R_{L-W} + R_{TAT}$. In this case, the layer L is homogeneous, and the resistances R_{L-W} and R_{TAT} are proportional to $L-W$ and W, respectively. This assumption is valid due to the uncertainty of the parameter W. Fairly simple calculations allow obtaining the following expression for the current-voltage curve test structure, where current is an independent variable

$$U = \phi \ln\left(1 + \frac{I_{ScB}}{I_S}\right)\left[1 + \frac{L-W}{W}\left(1 + \frac{R_V I_{ScB}}{\phi \ln\left(1+\frac{I_{ScB}}{I_S}\right)}\frac{W}{L}\right)\right]. \quad (12)$$

If we reverse the dependence (11) and add the linear component $I = I_{TAT} + I_{ScB}$ to the current, then we can get a graph of the approximating dependence. This plot is shown in Fig. 8, b with a dotted line for parameter values $I_S = 1.2 \cdot 10^{-7}$ A $\cdot$ cm^{-2}; $R_V = 5.1\,\Omega$; $L = 2 \cdot 10^{-5}$ cm; $W = 0.95 \cdot 10^{-5}$ cm. The resulting saturation current value corresponds to the height of the BS $\varphi_B = 0.81$ eV. The value of the electron affinity in this case is 3.5 eV, which is close

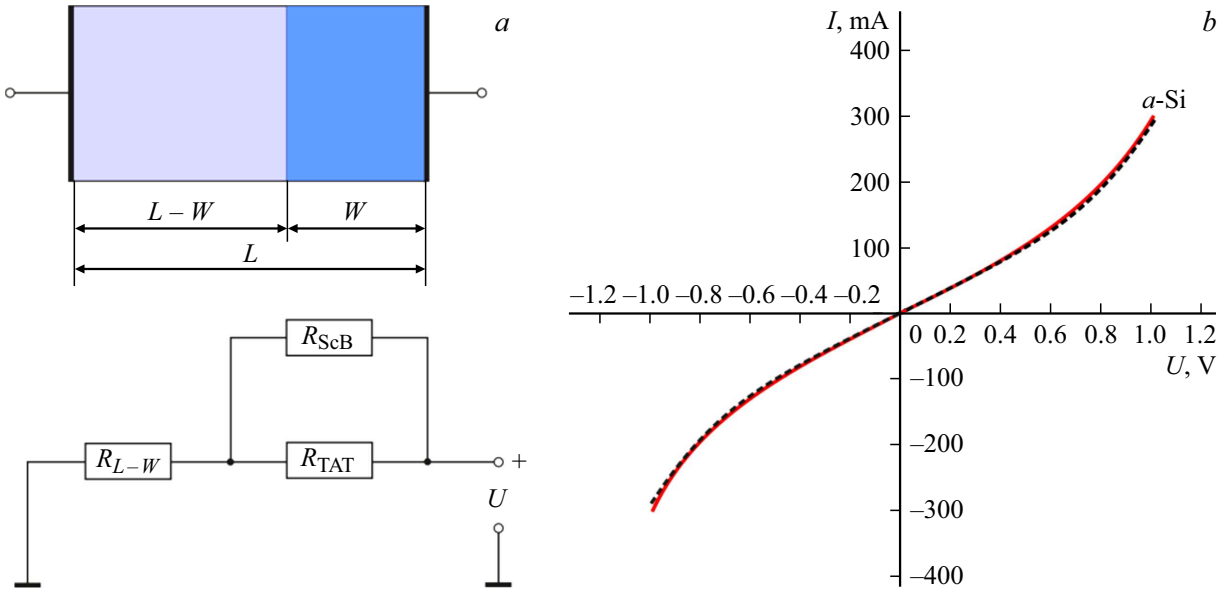

Figure 8. *a* — equivalent scheme of the test structure Ti—*a*-Si—Ti; *b* — approximating dependence (9) for parameter values $I_S = 1.2 \cdot 10^{-7}\,\mathrm{A \cdot cm^{-2}}$; $R_V = 5.1\,\Omega$; $L = 2 \cdot 10^{-5}\,\mathrm{cm}$; $W = 0.95 \cdot 10^{-5}\,\mathrm{cm}$.

enough to the literature data 3.93 eV for *a*-Si:H [26]. Note once again that the electron affinity is determined based on the Schottky–Mott $\chi = A_M - q\varphi_B$ rule, where A_M is taken as the average value of the output Ti, equal to 4.3 eV. Note also that the parameter W in general does not correspond to the width of the SCR. Such a correspondence is possible only if the resistivity of the segments $L-W$ and W is the same.

Returning to the Ti—Si@O@Al current-voltage curve, it should be noted that the absence of a tunneling current through an inversely displaced junction may mean a low density of tails of localized states in the mobility gap. It was noted in [4] that the solid solution *a*-$Si_{0.9}(Al_{0.1})$ in the composition of the Si@O@Al nanocomposite can be both an embedding solution and a substitution solution. In the latter case, Al, by analogy with hydrogen in *a*-Si:H passivates broken bonds. After transformation to sp^3-hybridized state, Al becomes embedded in the silicon crystal lattice, partially restoring its crystal structure. Due to the relatively small concentration of substitution atoms $10^{21}-10^{22}\,\mathrm{m^{-3}}$, the structure of *a*-$Si_{0.9}(Al_{0.1})$ remains amorphous, as evidenced by the results of X-ray diffractometry and Raman spectroscopy.

4.3. BAX Ti—*a*-$Si_{0.9}(Al_{0.1})$

At a low density of localized states of a solid solution *a*-$Si_{0.9}(Al_{0.1})$, its current-voltage curve, as well as the current-voltage curve Ti—Si@O@Al—Ti, should have the form of an exponent. Nevertheless, the current-voltage curve is linear in the entire measurement range from -1 to $+1$ V. The linearity of the current-voltage curve and the decrease of the band gap from $E_{g1} = 1.52 \pm 0.01$ eV to $E_{g3} = 0.8 \pm 0.003$ eV may be signs of semiconductor degeneracy *a*-$Si_{0.9}(Al_{0.1})$. The critical impurity concentration at which the valence and impurity zones merge is $6 \cdot 10^{26}\,\mathrm{m^{-3}}$ for silicon. The fraction of an electrically active impurity (substitution atoms) can reach several percent of the concentration of the dissolved component. Thus, at the concentration of aluminum $N_{Al} = 5.53 \cdot 10^{27}\,\mathrm{m^{-3}}$, the condition of zone fusion in *a*-$Si_{0.9}(Al_{0.1})$ can be met.

According to current-voltage curve on fig. 6, *b*, the resistance of the test structure is $R = 1.07\,\Omega$, which corresponds to the conductivity of $\sigma = 1.88 \cdot 10^{-3}\,\mathrm{S \cdot m^{-1}}$. At a critical concentration of impurity atoms, the mobility of holes is equal to $1.96 \cdot 10^{-11}\,\mathrm{m^2 \cdot V^{-1} \cdot s^{-1}}$, which is five orders of magnitude less than the Hall mobility of holes in *a*-Si:H $\mu = 1.2 \cdot 10^{-6}\,\mathrm{m^2 \cdot V^{-1} \cdot s^{-1}}$ [27]. This can be explained by the fact that in degenerate semiconductors, hopping charge transport by impurity localized states prevails. At the critical impurity concentration $6 \cdot 10^{26}\,\mathrm{m^{-3}}$, the average interatomic distance Al is 11.9 Å. Taking into account the spread of the impurity energy levels, the mobility may well be orders of magnitude less than the drift one.

The role of Al atoms, which are located in internodes, is less clear. Their concentration is nine times less than the concentration of silicon, and the average interatomic distance is 5.72 Å. These embedding atoms should form an impurity zone, so it is possible that the type of current-voltage curve is due to the conductivity of this zone, i.e. electron conductivity. However, this does not negate the fact of degeneration of *a*-$Si_{0.9}(Al_{0.1})$, which indicates a narrowing of the mobility gap. Then the hole conductivity of Si@O@Al can be explained only by reducing the concentration of Al in the *a*-Si(Al) phase to a value at which the embedding atoms do not form an impurity zone. A decrease of the concentration of an electrically active impurity simultaneously leads to the

removal of degeneracy, as indicated by the band gap Si@O@Al$E_{g1} = 1.52 \pm 0.01$ eV and $E_{g2} = 1.15 \pm 0.01$ eV.

4.4. BAX Ti—a-$SiO_{0.8}$

The current-voltage curve of the test structure Ti—a-$SiO_{0.8}$—Ti, as well as current-voltage curve Ti—a-Si—Ti, has a linear section. It is obvious that the nature of the ohmic section of the current-voltage curve is the same as that of amorphous silicon — tunneling through traps. At the boundaries of the linear section of the current-voltage curve, there is a tendency to reach saturation, which may be due to saturation of the drift conductivity. Unfortunately, it was not possible to investigate the current-voltage curve Ti—a-$SiO_{0.8}$—Ti in a wider voltage range due to electrical breakdown.

Summarizing the results obtained, it is necessary to note the adequacy of mathematical models approximating the current-voltage curve of test structures. By fitting the parameters of the approximating dependencies, the height of the SB for the contact of Ti with Si@O@Al and with silicon-containing phases of the nanocomposite was determined. It is shown that the approximation of the Si@O@Al current-voltage curve is possible only if the varistor effect is taken into account. An estimate of the electron affinity of Si@O@Al and a-Si was obtained based on the Schottky−Mott rule.

5. Discussion of findings

The obtained values of the band gap width should be compared with the values of E_g amorphous a-Si and hydrogenated a-Si:H silicon. According to the literature data, the width of the a-Si band gap is within 1.4−1.6 eV [28.29]. The width of the band gap a-Si:H varies widely from 1.55−1.58 [28] to 1.7 eV [19], i.e. adding the hydrogen as a rule, increases E_g, compared to a-Si [24]. The broadening of E_g into a-Si:H is explained by the shift of the maximum of the valence band „down“ as a result of the substitution of Si−Si bonds by a stronger bond Si−H [19]. The obtained value of the band gap Si@O@Al $E_g = 1.52$ eV lies in the range of values characteristic of both amorphous and amorphous hydrogenated silicon, but sharply differ from E_g solid solution a-$Si_{0.9}(Al_{0.1})$ ($E_g = 0.80$ eV).

The optical band gap in the studied films a-Si is 1.38 eV, which practically coincides with its lower boundary given in [26,28]. As a result of the addition of ~ 10 at.% Al, the optical band gap decreases to 0.80 eV, and amorphous silicon becomes a degenerate semiconductor with metallic conductivity. The coefficients of reflection and absorption of light change accordingly. Oxidation of a-Si to $SiO_{0.8}$ leads to an increase of the band gap to $E_g = 1.89$ eV, which is significantly less than the optical band gap of SiO_2, which is 3 eV [29]. The addition of Al to $SiO_{0.8}$, as in the case of a-Si, reduces E_g, but not so radically, but to a value of 1.52 eV. It is noteworthy that, the measurement results give only two values E_g due to the heterogeneity of the nanocomposite corresponding to amorphous $E_g = 1.52$ eV and nanocrystalline $E_g = 1.15$ eV silicon. No linear sections corresponding to other Si@O@Al components are observed on Tautz's plots. Thus, the obtained values of the band gap of the main phases of the Si@O@Al nanocomposite correspond to the literature data.

As already noted, in a solid solution a-$Si_{0.9}(Al_{0.1})$, the dissolved component Al can be located both in the interstices and in the nodes of the crystal lattice. In the second case, it is an alloying impurity that increases the hole conductivity of amorphous silicon. The linearity of the current-voltage curve a-$Si_{0.9}(Al_{0.1})$, the small value of E_g, intense light absorption and high concentrations of holes $9.79 \cdot 10^{22}\,m^{-3}$ indicate that a-$Si_{0.9}(Al_{0.1})$ — amorphous degenerate semiconductor. Therefore, Si@O@Al is a composite material with a varistor effect, in which the local concentration of Al can vary greatly, forming regions of different conductivity from metallic to intrinsic conductivity. The regions of high conductivity are a filler, whereas the regions of low conductivity, as well as pores, molecular clusters of SiO_2 and other dielectric phases play the role of a dispersant. As already noted, X-ray diffractograms Si@O@Al contain reflexes nc-Si(Al), which are most likely formed as a result of local ordering of the structure during passivation of broken bonds by sp^3-hybridized Al. Particles a-Si(Al) form a percolation cluster, the conductivity of which determines the characteristics of Si@O@Al current-voltage curve [5].

Returning to the purpose of this paper — construction of the band structure of the Ti—Si@O@Al contact, it is necessary to estimate the Fermi energy and the electron affinity of the nanocomposite. The minimum possible value of $E_g = 0.80$ eV should be taken as a band gap width and take its maximum possible value of $\chi = 3.3$ eV should be taken as the value of the electron affinity. Then, it is possible to write the condition $E_{FS} \geq -4.1$ eV taking into account $E_{FS} \simeq E_{VS}$ for the Fermi energy Si@O@Al. During the operation of the titanium output $A_{Ti} = 4.3$ eV, BS $q\varphi = E_{FM} - \chi \geq 1$ eV is formed in the area of the Ti—Si@O@Al contact. The barrier height was 2 eV in [4,5] based on model calculations [6,7], which does not contradict the results of this study. Thus, the model of step formation on silicon-based STLIB charging curves proposed in [4] is correct, and the cause of the voltage surge is lithium compensation of the donor impurity Al.

Conclusion

New data on the band structure of the Si@O@Al nanocomposite were obtained as a result of the study. The band gap width is determined and the electron affinity of the nanocomposite and the silicon-containing phases forming it is estimated. It is shown that Si@O@Al is a nanocomposite

material with a percolation (varistor) effect. Percolation clusters form a-Si(Al) phases with hole conductivity separated by dielectric phases and pores. The Si@O@Al band structure in the nanocomposite volume and in the metal contact area is mainly determined by the a-Si(Al) phase. The obtained band structure data allow concluding that the lithiation of Si@O@Al during the charging process leads to compensation of the acceptor impurity Al and changes in the band structure of the nanocomposite, its conductivity and the characteristics of the metal−Si@O@Al transition. These properties of Si@O@Al should be taken into account when designing STLIB and developing an algorithm for controlling the charge−discharge process.

Acknowledgments

Equipment provided by the „Diagnostics of Micro- and Nanostructures“ common use center was used in the study.

Funding

The study was supported financially by the Ministry of Science and Higher Education of the Russian Federation under state assignment №0856-2020-0006 for the Demidov Yaroslavl State University.

Conflict of interest

The authors declare that they have no conflict of interest.

References

[1] X. Yu, J. Bates, G. Jellison, F. Hart. J. Electrochem. Soc., **144** (2), 524 (1997). DOI: 10.1149/1.1837443

[2] A.A. Mironenko, I.S. Fedorov, A.S. Rudy, V.N. Andreev, D.Yu. Gryzlov, T.L. Kulova, A.M. Skundin. Monatshefte fur Chemie-Chemical Monthly, **150** (10), 1753 (2019). DOI: 10.1007/s00706-019-02497-1

[3] T.L. Kulova, A.A. Mironenko, A.S. Rudy, A.M. Skundin, *All Solid State Thin-Film Lithium-Ion Batteries. Materials, Technology, and Diagnostics* (CRC Press, Boca Raton, 2021), DOI: 10.1201/9780429023736

[4] A.S. Rudyi, A.A. Mironenko, V.V. Naumov, A.B. Churilov. Pis'ma v ZHTF, **48** (12), 32 (2022) (in Russian). DOI: 10.21883/PJTF.2022.12.52676.19188.

[5] A.S. Rudy, A.B. Churilov, A.A. Mironenko, V.V. Naumov, S.V. Kurbatov, E.A. Kozlov. Pis'ma v ZHTF, **48** (17), 9 (2022) (in Russian). DOI: 10.21883/PJTF.2022.17.53279.19276

[6] D.A. Drabold, U. Stephan, J. Dong, S.M. Nakhmanson. J. Mol. Graphics Mod., **17** (5−6), 285 (1999). DOI: 10.1016/S1093-3263(99)00036-4

[7] B.A. Golodenko, A.B. Golodenko. Vestn. Voronezh. Gos. Univ. Inzh. Tekhnol., **2**, 65 (2014) (in Russian). https://cyberleninka.ru/article/n/modelirovanieelekt-ronnoy-struktury-i-raschyot-osnovnyh-elektro-fizicheskihpa-rametrov-amorfnogo-kremniya

[8] J. Tauc, R. Grigorovic, A. Vancu. Phys. Stat. Sol. (b), **15** (2), 627 (1966). DOI: 10.1002/pssb.19660150224

[9] D.E. Aspnes, A.A. Studna. Phys. Rev. B, **27** (2), 985 (1983). DOI: 10.1103/PhysRevB.27.985

[10] A.P. Babichev, N.A. Babushkina, A.M. Bratkovsky, M.E. Brodov, M.V. Bystrov, B.V. Vinogradov, L.I. Vinokurova, E.B. Gelman, A.P. Geppe, I.S. Grigoryev, K.G. Gurtovoy, V.S. Egorov, A.V. Eletsky, L.K. Zarembo, V.Y. Ivanov, V.L. Ivashintseva, V.V. Ignatiev, R.M. Imamov, A.V. Inyushkin, N.V. Kadobnova, I.I. Karasik, K.A. Kikoin, V.A. Krivoruchko, V.M. Kulakov, S.D. Lazarev, T.M. Lifshits, Yu.E. Lubarsky, S.V. Marin, I.A. Maslov, E.Z. Meilikhov, A.I. Migachev, S.A. Mironov, A.L. Musatov, Yu.P. Nikitin, L.A. Novitsky, A.I. Obukhov, V.I. Ozhogin, R.V. Pisarev, Yu.V. Pisarevsky, V.S. Ptuskin, A.A. Radzig, V.P. Rudakov, B.D. Summ, R.A. Sunyaev, M.N. Khlopkin, I.N. Khlustikov, V.M. Cherepanov, A.G. Chertov, V.G. Shapiro, V.M. Shustriakov, S.S. Yakimov, V.P. Yanovsky. *Fizicheskie velichiny: Spravochnik.* Ed. by I.S. Grigor'ev, E.Z. Meilikhov (Energoatomizdat, M., 1991) (in Russian).

[11] W. Jacob, A. von Keudell, T. Schwarz-Selinger. Braz. J. Phys., **30** (3), 508 (2000). DOI: 10.1590/S0103-97332000000300006

[12] I.P. Herman. *Optical Diagnostics for Thin Film Processing* (Academic Press, NY., 1996), DOI: 10.1016/B978-0-12-342070-1.X5000-1

[13] Yu.I. Ukhanov. *Opticheskiye svoystva poluprovodnikov* (Nauka, M., 1977) (in Russian).

[14] L.P. Pavlov. *Metody izmereniya parametrov poluprovodnikovyh materialov* (Vysshaya shkola, M., 1987) (in Russian).

[15] M.N. Solovan, V.V. Brus, E.V. Maistruk, P.D. Maryanchuk. Inorg. Mater., **50** (1), 40 (2014). DOI: 10.1134/S0020168514010178

[16] Z. Ghorannevis, E. Akbarnejad, M. Ghoranneviss. J. Theor. Appl. Phys., **10**, 25 (2016). DOI: 10.1007/s40094-016-0219-7

[17] M.F. Hasaneen, Z.A. Alrowaili, W.S. Mohamed. Mater. Res. Express, **7** (1), 016422 (2020). DOI: 10.1088/2053-1591/ab6779

[18] M. Cesaria, A.P. Caricato, M. Martino. Appl. Phys. Lett., **105** (3), 031105 (2014). DOI: 10.1063/1.4890675

[19] R.A. Street. *Hydrogenated Amorphous Silicon* (Cambridge University Press, Cambridge, 1991), DOI: 10.1017/CBO9780511525247

[20] F.L. Martínez, A. Prado, I. Mártil, G. González-Díaz, B. Selle, I. Sieber. J. Appl. Phys., **86** (4), 2055 (1999). DOI: 10.1063/1.371008

[21] D.E. Carlson, C.R. Wronski. Appl. Phys. Lett., **28** (11), 671 (1976). DOI: 10.1063/1.88617

[22] L.A. Mazaletsky *Issledovaniye vliyaniya struktury i fazovogo sostava nanokompozitov na osnove kremniya na protsessy vnedreniya i ekstraktsii litiya.* Kand. diss. (MIFI, Moscow, 2022) (in Russian).

[23] T. Searle (ed.). *Properties of Amorphous Silicon and its Alloys* (London, INSPEC, IEE, 1998)

[24] E.V. Parinova. *Elektronno-energeticheskoe stroenie i fazovyj sostav amorfnyh nanokompozitnyh plenok a-SiO_x−a-Si:H.* Kand. diss. (VGU, Voronezh, 2016) (in Russian).

[25] J. Racko, J. Pecháček, M. Mikolášek, P. Benko, A. Grmanová, L. Harmatha, J. Breza. Radioengineering, **22** (1), 240 (2013).

[26] C.I. Ukan, R.V. Kruzelecky, D. Racansky, S. Zukotynski, J.M. Perz. J. Non-Cryst. Solids, **103** (1), 131 (1988). DOI: 10.1016/0022-3093(88)90425-5

[27] S. Dinca, G. Ganguly, Z. Lu, E.A. Schiff, V. Vlahos, C.R. Wronski, Q. Yuan. Mat. Res. Soc. Symp. Proc., **762**, A7.1.1 (2003). https://core.ac.uk/reader/215686760
[28] R.J. Loveland, W.E. Spear, A. Al-Sharbaty. J. Non-Cryst. Solids, **13** (1), 55 (1974). DOI: 10.1016/0022-3093(73)90035-5
[29] S.S. Nekrashevich, V.A. Gritsenko. Phys. of the Solid State, **56** (2), 207 (2014). DOI: 10.1134/S106378341402022X

Translated by Ego Translating